

# PiT: Progressive Diffusion Transformer

Jiafu Wu<sup>\*1</sup>, Yabiao Wang<sup>\*2</sup>, Jian Li<sup>1</sup>, Jinlong Peng<sup>1</sup>  
Yun Cao<sup>1</sup>, Chengjie Wang<sup>1</sup>, Jiangning Zhang<sup>2</sup>

<sup>1</sup>YouTu Lab, Tencent

<sup>2</sup>Zhejiang University

## Abstract

Diffusion Transformers (DiTs) achieve remarkable performance within image generation via the transformer architecture. Conventionally, DiTs are constructed by stacking serial isotropic global modeling transformers, which face significant quadratic computational cost. However, through empirical analysis, we find that DiTs do not rely as heavily on global information as previously believed. In fact, most layers exhibit significant redundancy in global computation. Additionally, conventional attention mechanisms suffer from low-frequency inertia, limiting their efficiency. To address these issues, we propose Pseudo Shifted Window Attention (PSWA), which fundamentally mitigates global attention redundancy. PSWA achieves moderate global-local information through window attention. It further utilizes a high-frequency bridging branch to simulate shifted window operations, which both enrich the high-frequency information and strengthen inter-window connections. Furthermore, we propose the Progressive Coverage Channel Allocation (PCCA) strategy that captures high-order attention without additional computational cost. Based on these innovations, we propose a series of Pseudo Progressive Diffusion Transformer (PiT). Our extensive experiments show their superior performance; for example, our proposed PiT-L achieves 54% $\uparrow$  FID improvement over DiT-XL/2 while using less computation.

## Introduction

Diffusion Transformer (DiT) (Peebles and Xie 2023) first utilize the Transformer as the basic architecture of the generation network. The time step and other conditions are injected into the Transformer blocks in the form of scale-shift (Peebles and Xie 2023) or cross-attention (Chen, Fan, and Panda 2021) to guide the diffusion generation trajectory. However, the introduction of the Transformer into the domain of vision generation by DiT is inelegant. DiT completely discards the U-Net (Ronneberger, Fischer, and Brox 2015) architecture that predominantly consists of convolutions in previous works, and instead fully employs the Transformer (Vaswani et al. 2017) blocks for global modeling. Although scaling up the model achieves state-of-the-art performance, this naturally raises an important question: Are such extensive global computations truly necessary in Diffusion Transformers?

To explore the dependence distance of diffusion full-size attention, we calculate the average tokens’ attention distance in each DiT layer. Figure 1 reveals that for a 16 $\times$ 16 latent map, 99% of tokens attend to neighbors within a row/column distance of 2-6 (see Equation 4 for distance metric). Thus DiT does not rely on long-distance attention modeling. Inspired by this finding, we re-evaluate the effect of restricting the Transformer’s scope, a strategy that drastically reduces computational overhead. We introduce *Static Window Attention* (Equation 5), which constrains tokens to calculate dependencies only within their local window. Our experiments reveal that, even with an identical macro architecture, the window attention mechanism leads to superior performance, thereby confirming our initial conjecture.

Another challenge is how to establish information connections between different windows. In Swin Transformer (Liu et al. 2021), the shifted window approach is a classic method of supplementing window connections. As illustrated in Figure 2 (a) and (b), by shifting or overlap, the windows create overlapping regions, effectively establishing window connections. However, these methods come with a substantial computational cost, as the model expends excessive computational resources in the overlapping areas.

Furthermore, as shown in Figure 3, we observe that the transformer in DiT excessively over-learns low-frequency information in the latent space, while lacking high-frequency details. To compensate for the deficiency of high-frequency information and establish a global information bridge between windows, we propose a novel *Pseudo Shifted Window Attention (PSWA)* (Equation 6, 7). As illustrated in Figure 4 and Figure 2(c), each block is divided into a static window attention branch and a high-frequency bridging branch constructed by depthwise separable convolution(DWConv). The high-frequency bridging branch not only supplements high-frequency information but also cleverly covers the edge regions of the static windows, constructing a bridge between windows to supplement information integration.

Moreover, we define conventional self-attention as first-order attention (Equation 10), which describes the pairwise similarity between tokens themselves. As shown in Figure 5, first-order similarity(see in Equation 9) tends to bias of low-level feature such as color and texture and fail to capture the intrinsic relationships among tokens. To address

<sup>\*</sup>These authors contributed equally.

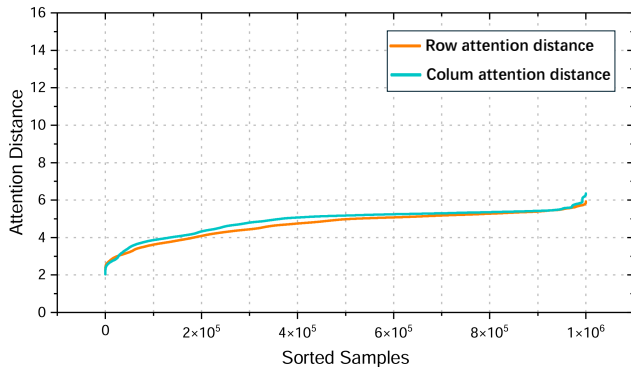


Figure 1: Row and column attention distance distribution. We sample one million samples to compute row and column attention distances from DiT’s attention maps. With a map edge length of 16, 99% of tokens have row and column attention distances under 6, indicating low long-distance attention demand and high computational redundancy.

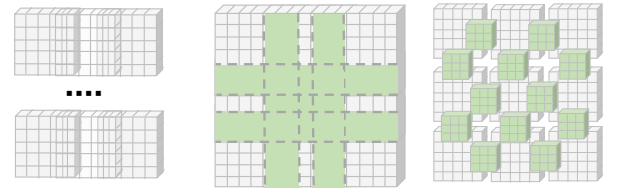
it, we propose a novel **Progressive Coverage Channel Allocation (PCCA)** strategy to capture **Kth-order attention** (Equation 10) without any additional computational cost. Our proposed Kth-order attention has a more effective attention mechanism than first-order attention.

In summary, our main contributions are as follows: (1) We observe that Diffusion Transformers DiT does not rely on long-distance attention modeling as traditionally assumed, and propose a **Static Window Attention** to mitigate the computational redundancy. (2) We propose the **Pseudo Shifted Window Attention (PSWA)**, introducing a high-frequency bridging branch to supplement information connection between windows while alleviating the overlearning of low-frequency information issue. (3) We pioneer the concept of Kth-order attention in vision generation and propose a novel **Progressive Coverage Channel Allocation (PCCA)** strategy to effectively capture **Kth-order attention** without additional computational cost. (4) Extensive experiments demonstrate that PiTs surpass state-of-the-art models in both isotropic and U-shape architectures. Ablation studies further validate the effectiveness and rationality of our proposed components.

## Related Work

### Vision Transformers

The emergence of Vision Transformers (ViT) (Dosovitskiy et al. 2020) redefines computer vision by challenging the dominance of Convolutional Neural Networks (CNNs) (He et al. 2016). ViT tokenizes images and employs positional encoding to retain inductive bias, demonstrating its effectiveness in large-scale image classification through a modular, layered design. Subsequent advancements, including DeiT (Touvron et al. 2021), PVT (Wang et al. 2021), and T2T (Yuan et al. 2021), have extended ViT’s capabilities to diverse vision tasks. Additionally, hybrid architectures such as CvT (Wu et al. 2021), CoatNet (Dai et al. 2021), ViTAE (Xu et al. 2021), and EMO series (Zhang et al.



(a) Shifted window (b) Window overlap (c) Pseudo shifted

Figure 2: Different window movement mechanisms. (a) sliding windows to create overlapping regions; (b) expanding window areas to form overlaps (green area); (c) parallel high-frequency bridging branches between windows via  $n \times n$  depthwise separable convolutions.

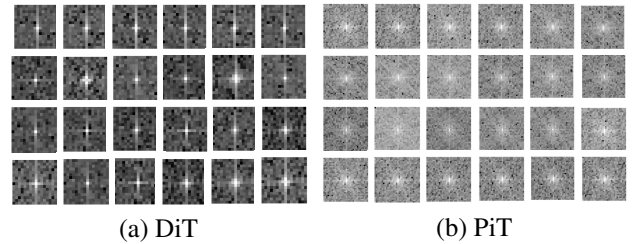


Figure 3: The Fourier transform frequency maps from DiT and PiT across different layers. In each image, the center represents low-frequency components, while the surrounding areas represent high-frequency components. The brightness and darkness variations indicate the magnitude of these components. Figure (a) illustrates DiT’s heavy reliance on low-frequency information, lacking high-frequency details. Figure (b) demonstrates that the PSWA enables the model to adequately capture both high- and low-frequency information, resulting in richer image details.

2023, 2024) integrate CNN and Transformer paradigms, further enhancing model efficiency and performance. More recently, Transformers have been adapted for multimodal vision perception, as exemplified by CLIP and GLIP, highlighting their versatility across vision tasks. Broadly, these vision models can be categorized into two architectural paradigms: isotropic (Dosovitskiy et al. 2020) and pyramid (Wang et al. 2021).

### Diffusion Transformers

Vision Transformers (ViTs) are widely employed in denoising models (Ho, Jain, and Abbeel 2020). Isotropic transformer architectures, such as IPT (Chen et al. 2021) and recent studies (Lu et al. 2024; Chu et al. 2024), have been applied to the same low-level vision generation tasks. Additionally, several diffusion models (Rombach et al. 2022; Esser et al. 2024) adopt a U-Net-based framework, integrating transformer blocks in a bottleneck configuration to achieve superior performance. DiT (Peebles and Xie 2023) and U-DiT (Tian et al. 2024) pioneer fully transformer-based architectures for diffusion models, employing transformers as denoisers. However, these models primarily focus on macro-level architectural design, with their core to-

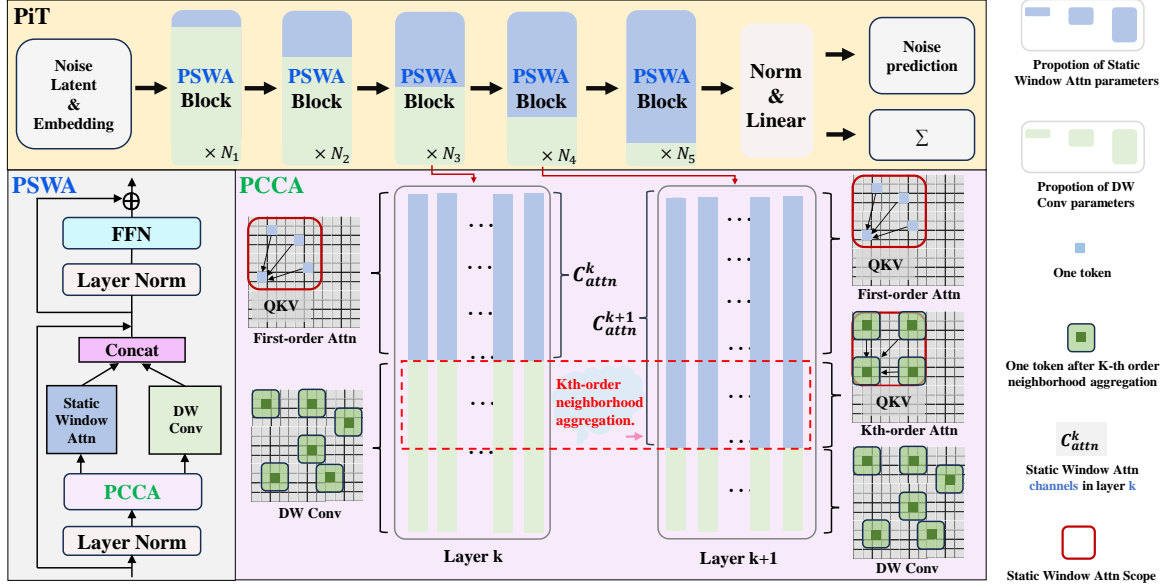


Figure 4: The overall framework of PiT. The static window attention and DWConv are the core operations of the PSWA Blocks. We also employ the Progressive Coverage Channel Allocation (PCCA) strategy with increasing proportions for the static window attention branch to introduce Kth-order attention.

ken interaction patterns directly inherited from ViT, lacking further exploration. Subsequent research on diffusion transformers (Gao et al. 2023a; Bao et al. 2023) explores training strategies and diffusion techniques, while FiT (Lu et al. 2024) and VisionLLaMA (Chu et al. 2024) enhance DiT by incorporating large language model techniques (Liu et al. 2025; Shazeer 2020). This suggests that the core attention mechanism in DiT has remained largely unchanged.

## Method

### Revisiting the Diffusion Transformers

Defining  $\mathbf{x}_t \in \mathbb{R}^{n \times d}$  as the noisy input at time step  $t$ . In the reverse denoising process,  $\mathbf{x}_{t-1}$  is formulated as:

$$\mathbf{x}_{t-1} = \boldsymbol{\mu}_\theta(\mathbf{x}_t, t) + \boldsymbol{\Sigma}_\theta^{1/2}(\mathbf{x}_t, t)\boldsymbol{\epsilon}, \quad \boldsymbol{\epsilon} \sim \mathcal{N}(\mathbf{0}, \mathbf{I}), \quad (1)$$

where  $\boldsymbol{\mu}_\theta$  and  $\boldsymbol{\Sigma}_\theta$  are the predicted mean and covariance matrix by Diffusion Transformer blocks.

At the microscopic level, for a layer  $l$  with the hidden state  $\mathbf{h}_l \in \mathbb{R}^{n \times d}$ , the Diffusion Transformer Block can be expressed as:

$$\mathbf{h}'_l = \mathbf{h}_l + \text{MHSA}(\text{Norm}(\mathbf{h}_l; t)), \quad (2)$$

$$\mathbf{h}_{l+1} = \mathbf{h}'_l + \text{FFN}(\text{Norm}(\mathbf{h}'_l; t)), \quad (3)$$

where MHSA is the multi-head self attention mechanism.

### Exploring the Intrinsic Dependence Distance

We carefully study the tokens dependence distance in the Multi-Head Self-Attention (MHSA) part of DiT. Specifically, we quantify the mean dependence distance across attention maps during batch generation with a pre-trained DiT-B/2. For a single-head attention map, we formally define the

row and column attention distance as:

$$D_{\text{row}}(\mathbf{A}) = \frac{\sum_{i,j} |\mathbf{r}_j - \mathbf{r}_i| \cdot A_{ij}}{\sum_{i,j} A_{ij}}, \quad (4)$$

$$D_{\text{col}}(\mathbf{A}) = \frac{\sum_{i,j} |\mathbf{c}_j - \mathbf{c}_i| \cdot A_{ij}}{\sum_{i,j} A_{ij}},$$

where  $A_{ij}$  denotes the similarity (*cosine*) between token  $i$  and token  $j$  in the attention map, and  $\mathbf{r}_i$  is the row number of token  $i$ ,  $\mathbf{c}_i$  is the column number of token  $i$ .

We randomly evaluate the attention distances across one million attention maps. As depicted in Figure 1, when the spatial height and width of the map in the shallow layer are both 16, the majority of rows and columns attention distances fall within the range of 2 to 6, well below the maximum limit of 16. This observation suggests that the global information reliance of DiT is less obvious than previously assumed, and the rapid convergence of DiT is predominantly driven by local information.

Therefore, we suggest using the *Static Window Attention* mechanism in the diffusion framework, which offers a balanced dependency range and computational efficiency.

$$\text{WinAttn}(X) = \bigcup_w \left( \frac{Q_w K_w^\top}{\sqrt{d}} + P_w \right) V_w, \quad (5)$$

where  $X$  is the input,  $Q_w$ ,  $K_w$ , and  $V_w$  are the linear transformation outputs of  $X$  in the window  $w$ .  $P_w$  is the positional encoding within window  $w$ .

### Pseudo Shifted Window Attention (PSWA)

While the window attention in Equation 5 successfully reduces global computational redundancy, two critical chal-

lenges remain: (1) inter-window information exchange, and (2) the inherent low-frequency bias in attention mechanisms.

**Connecting different windows.** It is crucial to establish information connections between different window attention mechanisms. Figure 2 (a) and (b) illustrate that connections between windows can be supplemented by sliding windows or increasing the window area to create overlaps between windows. However, both methods cause the model to consume a large amount of computational resources in the overlapping regions, and they are not the optimal choices.

**Attention mechanism has a low-frequency bias.** We observe that DiT exhibits a strong bias toward low-frequency information in generative tasks. As illustrated in Figure 3(a), the DiT feature maps from pure attention show rich low frequencies in the frequency domain, emphasizing macro structures but ignoring detailed and fine-grained information.

To establish informational bridges between windows and supplement high-frequency detail information, we propose a novel Pseudo Shifted Window Attention (PSWA) mechanism. As illustrated in the PSWA part of Figure 4, the image features are split into two components in the channel space: one is the static window attention branch, and the other is the high-frequency bridging branch via depthwise separable convolution (DWConv). Mathematically, PSWA can be described as follows:

$$\text{PSWA}(X) = \text{FFN}(\text{Norm}((f(\text{Norm}(X)) + X))) + X \quad (6)$$

$$f(X) = \text{Concat}(\text{WinAttn}(X_{\text{attn}}), \text{DWConv}(X_c)) \quad (7)$$

where  $X$  is the input, and it is split into two parts at the channel level:  $X_{\text{attn}}$  is used for the window attention branch, and  $X_c$  is used for the high-frequency bridging branch (DWConv). Norm is the Layer Norm layer, and FFN is the feed-forward network (linear layer).

Figure 2(c) better illustrates how PSWA connects different static windows from the pixel perspective. The dense convolution kernels will always have many falling on the adjacent boundaries of different windows (the green part in figure 2(c)), and they effectively connect different windows. Additionally, Depthwise Convolution (DWConv) is known for its strong high-frequency extraction capabilities. As depicted in Figure 3(b), when PSWA uses DWConv to connect windows, it significantly supplements high-frequency details in the frequency domain. It is also important to note that adding this high-frequency bridging branch to PSWA does not increase the computational cost. The computational cost for this channel is inherent in the attention mechanism, and replacing it with DWConv actually leads to a reduction in computation.

### Progressive Coverage Channel Allocation (PCCA)

Before introducing Progressive Coverage Channel Allocation (PCCA), we first need to present three important new concepts: Kth-order neighborhood, Kth-order similarity and Kth-order attention.

**Kth-order neighborhood.** Considering an input sequence represented as a set of points. For any position  $i$  in this sequence, we define its Kth-order neighborhood  $\mathcal{N}_K(i)$

as the set of positions  $j$  that satisfy the spatial condition:

$$\mathcal{N}_K(i) \triangleq \{j \mid \max(|x_j - x_i|, |y_j - y_i|) \leq K - 1\} \quad (8)$$

where  $x$  and  $y$  are the coordinate components of positions  $i$  and  $j$ . To put it simply, the Kth-order neighborhood of a central node ‘ $i$ ’ comprises the nodes within the  $(K-1)$  surrounding layers.

**Kth-order similarity.** Assuming an aggregation function  $\Phi$  that processes the Kth-order neighborhood to one feature representation. The Kth-order similarity between positions  $i$  and  $j$  is then defined as:

$$S_K(i, j) \triangleq \langle \Phi(\mathcal{N}_K(i)), \Phi(\mathcal{N}_K(j)) \rangle, \quad (9)$$

where  $\langle \cdot, \cdot \rangle$  is the inner product operation, and  $\Phi$  is a **Kth-order neighborhood aggregation mapping** (e.g., DWConv). If  $K = 1$ , the Kth-order similarity degenerates to the **first-order similarity**.

**Kth-order attention.** Kth-order attention is an attention mechanism that calculates the attention map using Kth-order similarity, and its mathematical definition is as follows:

$$\text{Attn}_K(X) = (S_K + P) V. \quad (10)$$

where  $X$  is the input,  $S_K$  is the similarity map computed by the Kth-order similarity in Eq. 9,  $P$  is the positional encoding, and  $V$  is the output of  $X$  after a linear layer. If  $K = 1$ , the Kth-order attention degenerates to **first-order attention**.

The first-order similarity only measures the similarity of the tokens themselves, not considering the similarity of their neighboring tokens. The first-order similarity may be inadequate for capturing the intricate, high-level relationships between tokens. As shown in Figure 5, this measure is biased towards low-level features such as color and texture. In Figure 5, the two black nodes: one is a part of the dog’s fur, and one is a part of the street lamp. They show extremely high similarity both in pixel space and latent space. However, they belong to completely different categories and should not exhibit such a strong similarity dependency. It means that two tokens with similar color and texture but no semantic relationship will exhibit a strong correlation, while tokens with meaningful semantic connections but differing low-level features are often disregarded in the diffusion transformer layers. This limitation compromises the semantic consistency of the generated images or videos.

In contrast, the Kth-order similarity is more semantic, as it doesn’t merely describe the similarity of the tokens themselves but rather measures the feature similarity of the surrounding neighbors of the central token. The Kth-order similarity can effectively make up for the shortcomings of the first-order similarity. It encourages attention connections where both the tokens themselves and their neighbors are similar, and simultaneously penalizes the misleading attention connections where the tokens are similar to each other but dissimilar to their surrounding neighbors. For example, as shown in Figure 5, when we consider the neighbors within two hops around the black nodes, the feature difference becomes apparent. In other words, the third-order similarity between these two black nodes is very low.

**Capturing Kth-order similarity.** The higher-order similarity with a larger similarity receptive field needs more

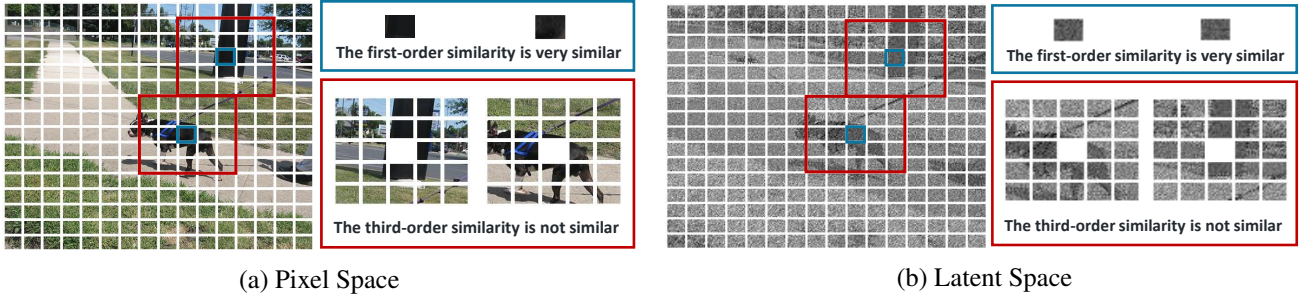


Figure 5: The first-order similarity measure tends to prioritize low-level features such as color and texture. As illustrated by the blue box, two black image patches appear similar in their low-level features, even though one represents a dog’s fur and the other a roadside post. The first-order similarity measure thus leads to a strong correlation between them, potentially misleading the model. In contrast, when higher-order similarity is considered, as shown in the red box, the expanded receptive field captures the semantic differences between these patches.

complex calculations. An intuitive way to capture it is to design a special module to additionally calculate the Kth-order similarity, but this will introduce an extra computational burden to the model.

To capture Kth-order similarity without incurring additional computational overhead, we ingeniously introduce a Progressive Coverage Channel Allocation (PCCA) strategy based on the PSWA. As illustrated in PCCA part of Figure 4, the tokens of layer  $k$  are split into two branches at the channel space. The blue part is the static window attention, and it occupies  $C_{attn}^k$  channels. *The traditional attention within the window is equal to first-order attention*, as it captures the similarity of the tokens themselves within the window. The other part of the channels is the high-frequency bridging branch. It is implemented by DWConv and mainly captures local and high-frequency information.

**The key insight of PCCA is as follows: As the model layer goes deeper, the channel proportion of the static window attention branch increases, and the channel proportion of the high-frequency bridging branch decreases.**

In the shallow layers of the model, the channel proportion of the high-frequency bridging branch far exceeds that in the static window attention branch. As the model progresses deeper, the proportion of high-frequency bridging branch channels gradually decreases, and part of its channels are transferred to the static window attention branch. As illustrated in the PCCA part of Figure 4, in layer  $k + 1$ , the channels within the red dashed box are assigned to the static window attention branch. The tokens in these channels have already absorbed sufficient local information from their surrounding neighborhood in layer  $k$ . Taking the high-frequency bridging branch with a  $5 \times 5$  DWConv as an example, the channels in the red area have already captured features from the third-order neighborhood in layer  $k$ . At this point, their features represent not only themselves, but also represent all tokens within the third-order neighborhood. When these channels are passed to the static window attention branch in layer  $k + 1$  to naturally compute first-order similarity, the result is no longer a simple first-order similarity, but rather third-order similarity. The mathemat-

cal expression is as follows:

$$S_{ij}^3 = \sum_c^{C_{attn}^{k+1} - C_{attn}^k} (Conv_5(X_i^c) \cdot Conv_5(X_j^c)), \quad (11)$$

where  $C_{attn}^k$  denotes the channels of window attention in the layer  $k$ , while  $C_{attn}^{k+1}$  denotes the channels of window attention in the layer  $(k + 1)$ .  $Conv_5$  is equal to the aggregation function  $\Phi$  in Equation 9.  $Conv_5(X_i^c)$  is the output of  $5 \times 5$  convolution at token  $i$ , channel  $c$ ; and  $Conv_5(X_j^c)$  is the output of  $5 \times 5$  convolution at token  $j$ , channel  $c$ .

## Experiments

Based on all the above investigations, we design a series of isotropic and U-shaped PiTs. To demonstrate the outstanding performance of PiTs, we conduct a lot experiments following the training settings of DiT: The Variational Autoencoder (VAE) employs sd-vae-ft-ema, the training batch size is set to 256, the optimizer is AdamW, the learning rate is set at  $1 \times e^{-4}$ , and all the hyperparameters in the comparative experiments are the same. The state-of-the-art methods involved in the experiment are as follows: DiT (Peebles and Xie 2023), MDT (Gao et al. 2023a), MDTv2 (Gao et al. 2023b), U-DiT (Tian et al. 2024), DiffTi (Hatamizadeh et al. 2024), and PixArt- $\alpha$  (Chen et al. 2023).

### Scaling the PiTs Up

We construct PiTs based on the core operation of PSWA, and scale up the models to compare them with larger-sized DiTs and some previous state-of-the-art (SOTA) models. For a fair comparison, the macro-architecture of PiT adopts a U-shaped (Tian et al. 2024), and the comparison of parameters and FLOPs with U-DiTs is shown in Table 1. All the models are trained for 400K iterations under the same parameter settings. Table 2 presents the results on the standard ImageNet with a size of  $256 \times 256$ , while Table 5 reports the results at a resolution of  $512 \times 512$ . In Table 2, it can be observed that PiT-B achieves an FID metric that is 24.1% better than that of DiT-XL/2 while having only 23.2% of the FLOPs of DiT-XL/2. PiT-B also shows an FID



Model	U-DiT-S	PiT-S	U-DiT-B	PiT-B	U-DiT-L	PiT-L
#Param.(M)	58.90	58.06	231.25	236.07	916.34	914.99
FLOPs(G)	7.15	7.08	26.55	25.56	102.11	100.80

Table 1: Comparison of model parameters and FLOPs.

Model	FLOPs(G)	FID ↓	sFID ↓	IS ↑	Prec. ↑	Rec. ↑
DiT-S/2	5.46	68.40	-	-	-	-
DiT-S/2*	5.46	67.87	9.63	20.16	0.350	0.536
MDT-S/2	6.06	53.46	-	-	-	-
MDTv2-S/2	6.06	39.50	-	-	-	-
U-DiT-S	7.15	31.51	8.97	51.62	0.543	<b>0.633</b>
PiT-S (Ours)	7.08	<b>29.89</b>	<b>8.78</b>	<b>53.28</b>	<b>0.550</b>	0.6231
DiT-B/2	21.82	43.47	-	-	-	-
DiT-B/2*	21.82	42.62	8.57	33.31	0.480	0.626
MDT-B/2	23.01	34.33	-	-	-	-
MDTv2-B/2	23.02	19.55	-	-	-	-
U-DiT-B	26.55	16.64	6.33	85.15	0.642	0.639
PiT-B (Ours)	25.56	<b>15.56</b>	<b>6.00</b>	<b>88.86</b>	<b>0.648</b>	<b>0.647</b>
U-ViT-L	76.40	21.22	6.10	67.64	0.615	0.633
DiffTi-XL/2	118.50	36.86	6.53	35.39	0.540	0.613
PixArt- $\alpha$ -XL/2	118.40	24.75	6.08	52.24	0.612	0.613
DiT-XL/2	114.46	19.47	-	-	-	-
DiT-XL/2*	114.46	19.86	6.19	66.97	0.634	0.622
MDT-XL/2	118.70	16.42	-	-	-	-
U-DiT-L	102.11	10.08	5.21	112.44	0.702	<b>0.631</b>
PiT-L (Ours)	100.80	<b>9.18</b>	<b>4.87</b>	<b>117.76</b>	<b>0.714</b>	0.620

Table 2: The comparison of various PiT sizes with state-of-the-art methods. The resolution is  $256 \times 256$ .

improvement of 6.5% compared to U-DiT-B. Additionally, PiT-L outperforms DiT-XL/2 by 10.68 in the FID metric with fewer FLOPs, which is almost twice the performance of DiT-XL/2. In contrast to the SOTA model U-DiT-L, PiT-L maintains 8.9% lead.

For a more detailed comparison, we carry out a step-by-step comparison between PiTs of both Base and Large sizes and the previous state-of-the-art (SOTA) methods. We respectively report their metrics at 200k, 400K, 600K, 800K, and 1M iterations. As can be seen from Table 3, the PiT-L with a smaller model size surpasses the metrics of DiT-XL/2 at 7M iterations when it reaches 1M iterations. The FID of PiT-L is 27.7% better, while the training cost is reduced by a factor of seven. When compared with U-DiT, PiT-B and PiT-L outperforms U-DiT-B and U-DiT-L at all iterations.

Model	FLOPs(G)	FID ↓	sFID ↓	IS ↑	Prec. ↑	Rec. ↑
DiT-S/2	5.46	68.40	-	-	-	-
DiT-S/2*	5.46	67.40	11.93	20.44	0.368	0.559
PiT-S/2 (Ours)	5.30	<b>61.24</b>	<b>10.37</b>	<b>23.02</b>	<b>0.380</b>	<b>0.576</b>
DiT-B/2	21.82	43.47	-	-	-	-
DiT-B/2*	21.82	42.84	8.24	33.66	0.491	0.629
PiT-B/2 (Ours)	20.13	<b>39.19</b>	<b>7.67</b>	<b>37.76</b>	<b>0.500</b>	<b>0.635</b>
DiT-L/2	77.53	23.33	-	-	-	-
DiT-L/2*	77.53	23.27	6.35	59.63	0.611	0.635
PiT-L/2 (Ours)	72.30	<b>21.25</b>	<b>5.72</b>	<b>65.41</b>	<b>0.724</b>	<b>0.638</b>

Table 4: The comparative experimental results of replacing Multi-Head Self-Attention (MHSA) with Pseudo Shifted Window Attention (PSWA) in DiTs (denotes \*).

Model	Steps	FID ↓	sFID ↓	IS ↑	Prec. ↑	Rec. ↑
DiT-XL/2	7M	9.62	-	-	-	-
U-DiT-B	200K	23.23	6.84	64.42	0.610	0.621
U-DiT-B	400K	16.64	6.33	85.15	0.642	0.639
U-DiT-B	600K	14.51	6.30	94.56	0.652	0.643
U-DiT-B	800K	13.53	6.27	98.99	0.654	0.645
U-DiT-B	1M	12.87	6.33	103.79	0.661	0.653
PiT-B (Ours)	200K	21.80	6.34	67.80	0.625	0.626
PiT-B (Ours)	400K	15.56	6.00	88.86	0.648	0.647
PiT-B (Ours)	600K	13.53	6.00	98.04	0.657	0.647
PiT-B (Ours)	800K	12.62	<b>5.96</b>	103.61	0.661	<b>0.654</b>
PiT-B (Ours)	1M	<b>11.83</b>	5.98	<b>108.33</b>	<b>0.663</b>	0.650
U-DiT-L	200K	15.26	5.60	86.01	0.685	0.615
U-DiT-L	400K	10.08	5.21	112.44	0.702	0.631
U-DiT-L	600K	8.71	5.17	122.45	0.705	0.645
U-DiT-L	800K	7.96	5.21	131.35	0.705	0.648
U-DiT-L	1M	7.54	5.27	135.49	0.706	0.659
PiT-L (Ours)	200K	13.76	5.09	90.49	0.693	0.612
PiT-L (Ours)	400K	9.18	4.87	117.76	0.714	0.620
PiT-L (Ours)	600K	7.91	4.91	128.24	<b>0.718</b>	0.635
PiT-L (Ours)	800K	7.25	4.87	134.15	0.716	0.641
PiT-L (Ours)	1M	<b>6.96</b>	<b>5.02</b>	<b>138.84</b>	0.714	<b>0.646</b>

Table 3: We performed a comprehensive evaluation of PiT models at various training iterations on the ImageNet-1K dataset with a resolution of  $256 \times 256$ . Across all iterations, our PiT models consistently achieved superior FID metrics compared to both DiT and U-DiT.

Model $512 \times 512$	Steps	FID ↓	sFID ↓	IS ↑	Prec. ↑	Rec. ↑
DiT-XL/2*	400K	21.07	6.80	66.14	0.741	0.575
U-DiT-B*	400K	15.62	6.82	<b>92.43</b>	0.751	0.601
PiT-B (Ours)	400K	<b>15.08</b>	<b>6.44</b>	90.04	<b>0.753</b>	<b>0.608</b>

Table 5: Comparing PiT against DiT and U-DiT on ImageNet  $512 \times 512$  generation.

Throughput↑ (imgs/s)	DiT-S/2	DiT-B/2	DiT-L/2
	497	272	104
	PiT-S/2	PiT-B/2	PiT-L/2
	<b>1225</b>	<b>618</b>	<b>248</b>

Table 6: Comparison of FP32 training throughput between DiTs and PiTs on the same GPUs.

To purely demonstrate the remarkable performance of the Pseudo Shifted Window Attention (PSWA), we conduct comparative experiments on the isotropic architecture of DiT by merely replacing the multi-head self-attention mechanism with PSWA, while keeping all the other structures and hyperparameters unchanged. As can be seen from Table 4, simply substituting the Multi-Head Self-Attention (MHSA) has achieved substantial improvements across models of different sizes. It is particularly worth noting that the computational cost of PSWA is lower compared to that of MHSA.

## Ablation Study

To explore whether the Kth-order attention is truly effective, we conduct ablation experiments on PiT-B at the channel level. All the experiments are trained for 200K iterations on ImageNet-1K. In Table 7,  $C_{win}$  denotes the channels in the static window attention branch, and  $C_{bridge}$  represents the high-frequency bridging branch channels. The first row of Table 7 indicates that the model without the core window attention and only with the bridging branch is the worst, with a FID of merely 29.15. The second row shows that the FID with only static window attention and no bridging branch is still only 23.29. The third row reveals that when the static window attention branch channels gradually decrease and the high-frequency bridging branch channels gradually increase (without absorbing the Kth-order attention), the FID is 22.92, which is still not very high. The fourth row demonstrates that when the channels of the two branches are divided equally, the result is only slightly better, with an FID of 22.83. The fifth row indicates that when the static window attention branch channels gradually increase and the high-frequency bridging branch channels gradually decrease (fully absorbs the information of the Kth-order neighborhood), achieving the best performance with an FID reaching 21.80.

PiT-B	FID ↓	sFID ↓	IS ↑	Prec. ↑	Rec. ↑
$C_{win} = 0, C_{bridge} = C$	29.15	7.51	58.46	0.610	0.607
$C_{win} = C, C_{bridge} = 0$	23.29	6.88	65.21	0.608	0.610
$C_{win}/C \downarrow, C_{bridge}/C \uparrow$	22.92	6.58	66.37	0.613	0.619
$C_{win}/C = C_{bridge}/C$	22.83	6.51	66.38	0.609	0.616
$C_{win}/C \uparrow, C_{bridge}/C \downarrow$	<b>21.80</b>	<b>6.34</b>	<b>67.8</b>	<b>0.625</b>	<b>0.626</b>

Table 7: Ablation study on ImageNet evaluating channel allocation strategies for the static window attention and high-frequency bridging branches, where all models were trained for 200K iterations.

We explore the influence of the range of K for the Kth-order attention, that is, the influence of the DWConv kernel-size (where kernel-size =  $2K - 1$ ). As shown in Table 8, when  $K=1$ , the model uses only first-order attention, resulting in the worst performance with an FID score of 17.53. Both  $K=2$  and  $K=5$  achieve the optimal FID value of 15.56. The Precision (Prec.) metric reaches its highest value of 0.656 when  $K=3$ , while the values for the other three cases are also comparable. Furthermore, the optimal values for the three metrics, namely sFID, Inception Score (IS), and Recall (Rec.), are all obtained when  $K=5$ .

PiT-B	FID ↓	sFID ↓	IS ↑	Prec. ↑	Rec. ↑
1st-order Attn	17.53	6.56	86.34	0.637	0.632
2nd-order Attn	<b>15.56</b>	6.02	88.48	0.648	0.631
3rd-order Attn	15.69	6.03	88.03	<b>0.656</b>	0.636
4th-order Attn	15.80	6.05	87.7	0.648	0.636
5th-order Attn	<b>15.56</b>	<b>6.00</b>	<b>88.86</b>	0.648	<b>0.647</b>

Table 8: Ablation study on the range K of Kth-order similarity. All results were trained on ImageNet-1K for 400K steps.

## Visualization

We visualize the results of U-DiT-B and PiT-B, with all models trained on ImageNet-1K for 400K iterations under the same training settings. As illustrated in Figure 6, PiT-B evidently exhibits superior detail and texture. For instance, in the first column, the generated image of the electric cooker by U-DiT-B appears blurred and indistinct. In contrast, PiT-B produces images with sharp and exquisite details. Figure 7 shows the process where the results generated by PiT-L get better and better as the training steps increase.



Figure 6: The comparison of image generation results among DiT-B/2, U-DiT-B, and PiT-B models. Owing to the high-frequency information provided by the bridging branch, PiT-B exhibits superior detail and texture. All images are from the ImageNet-1K dataset (Deng et al. 2009)

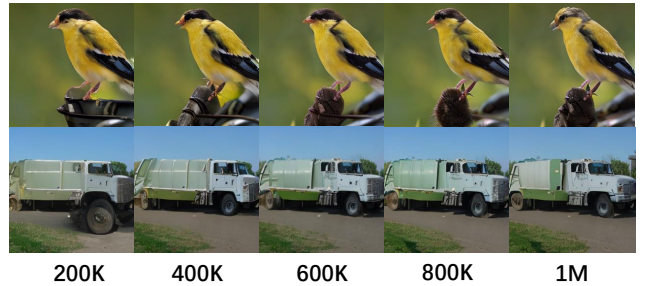


Figure 7: As training iterations increase, the generated images of PiT-L are richer in textural details. All images are from the ImageNet-1K (Deng et al. 2009)

## Conclusion

In this paper, we propose a novel Pseudo Shifted Window Attention (PSWA), which address the global computational redundancy issue and low-frequency bias in the Diffusion Transformer (DiT). PSWA has a high-frequency window bridging branch that operates in parallel with static window attention across channels. Furthermore, we introduce the concept of Kth-order Attention in the vision generative domain, elevating the traditional attention concept to a higher level. We also propose a novel Progressive Coverage Channel Allocation (PCCA) that captures high-order similarity information without any incurring additional computational cost. Our final method, named PiT, is extensively validated via quantitative and visualization experiments, which demonstrate its superior performance.

# Supplementary Material

## Insights on attention low-frequency bias

We propose the Propagation of Low-Frequency Theorem ??, and theoretically demonstrate that attention will fall into low-frequency bias regardless of the size of the overlapping region in window attention (with the maximum being full-size attention). Specifically, methods for connecting different windows, such as (a) sliding windows and (b) overlapping window regions (as shown in Figure 2), will both ultimately result in a low-frequency bias. PSWA is one of the few effective and robust approaches to tackle low-frequency bias.

**Theorem 1. Propagation of Low-Frequency.** Let  $\{\mathcal{A}_\rho\}_{\rho \in [0,1]}$  be a family of window attention operators with overlap ratio  $\rho$ . It is known that when  $\rho = 0$  or  $\rho = 1$ , the full-size attention exhibits low-frequency bias (Figure 3 (a) in of the main manuscript), which corresponds to the two boundary conditions:

$$\lim_{t \rightarrow \infty} \frac{\|\mathcal{F}(X^{(t)})\|_{\Omega_H}}{\|\mathcal{F}(X^{(t)})\|_{\Omega_L}} = 0 \quad (\text{No overlap } \rho = 0), \quad (12)$$

$$\lim_{t \rightarrow \infty} \frac{\|\mathcal{F}(X^{(t)})\|_{\Omega_H}}{\|\mathcal{F}(X^{(t)})\|_{\Omega_L}} = 0 \quad (\text{Full overlap } \rho = 1). \quad (13)$$

Where  $\Omega_H \triangleq \{\omega \in \mathbb{R}^d : \|\omega\|_2 > \beta_0\}$  represents the high-frequency region; and  $\Omega_L \triangleq \Omega \setminus \Omega_H$  represents the low-frequency region.  $\beta_0 > 0$  denotes the threshold separating high-frequency and low-frequency regions.

For the intermediate states where  $\rho \in (0, 1)$ , i.e., when there is a certain degree of overlap between window attentions, low-frequency bias is also exhibited:

$$\lim_{t \rightarrow \infty} \frac{\|\mathcal{F}(X^{(t)})\|_{\Omega_H}}{\|\mathcal{F}(X^{(t)})\|_{\Omega_L}} = 0. \quad (14)$$

### Proof of Theorem 1.

Defining the overlap mask matrix  $P_\rho$  with entries:

$$P_\rho(i, j) = \begin{cases} 1 & \text{if } |i - j| \leq m(1 + \rho) \\ 0 & \text{otherwise} \end{cases} \quad (15)$$

where  $\rho = 0$  represents no overlap between window attentions, and  $\rho = 1$  represents full overlap, i.e., full-size attention. The attention operator is:

$$\mathcal{A}_\rho(X) = P_\rho \odot \text{Softmax}\left(\frac{XX^\top}{\sqrt{d}}\right)X \quad (16)$$

where  $\odot$  denotes the Hadamard product. Let  $L(X) = I - \text{Softmax}\left(\frac{XX^\top}{\sqrt{d}}\right)$ . Through the Neumann series expansion:

$$\mathcal{A}_\rho(X) = [I - P_\rho \odot L(X)]X \quad (17)$$

Using the Fourier dynamics equation:

$$\mathcal{F}(X^{(t+1)}) = e^{-\gamma(\rho)\|\omega\|^2} \mathcal{F}(X^{(t)}) + \mathcal{N}(X^{(t)}) \quad (18)$$

we analyze the high-frequency energy at step  $t$ :

$$\|\mathcal{F}(X^{(t)})\|_{\Omega_H} \leq e^{-\gamma(\rho)\beta_0^2} \|\mathcal{F}(X^{(t-1)})\|_{\Omega_H} + \|\mathcal{N}(X^{(t-1)})\|_{\Omega_H} \quad (19)$$

In  $\Omega_L$ , where the linear damping term is weak ( $\|\omega\|_2 \leq \beta_0$ ), the equation approximates to:

$$\mathcal{F}(X^{(t+1)}) \approx \mathcal{F}(X^{(t)}) + \mathcal{N}(X^{(t)}) \quad (20)$$

Due to the normalization operation (Softmax) in the attention mechanism, the low-frequency energy remains non-decaying.  $\mathcal{N}(X^{(t)})$  in the low-frequency region satisfies:

$$\|\mathcal{N}(X^{(t)})\|_{\Omega_L} \leq C \|\mathcal{F}(X^{(t)})\|_{\Omega_L} \quad (21)$$

where  $C < 1$ , guaranteed by the normalization property of the attention weights. Defining the low-frequency energy  $E_L(t) = \|\mathcal{F}(X^{(t)})\|_{\Omega_L}$ , we have:

$$E_L(t+1) \geq E_L(t) - CE_L(t) \geq (1-C)E_L(t) \quad (22)$$

Recursively, we obtain:

$$E_L(t) \geq (1-C)^t E_L(0) \geq c > 0 \quad (23)$$

where  $c = \liminf_{t \rightarrow \infty} (1-C)^t E_L(0)$ , since  $(1-C)^t$  does not decay to zero when  $C < 1$ .

Continuing the analysis of the upper bound of high-frequency energy decay, under the smoothness assumption of the attention mechanism, the nonlinear term in the high-frequency region satisfies:

$$\|\mathcal{N}(X^{(t)})\|_{\Omega_H} \leq C\rho^2 \|\mathcal{F}(X^{(t)})\|_{\Omega_L}^2 \quad (24)$$

Given the lower bound of  $\|\mathcal{F}(X^{(t)})\|_{\Omega_L}$ , in the high-frequency region  $\Omega_H = \{\omega : \|\omega\|_2 > \beta_0\}$ , the linear damping term dominates, and the high-frequency part of the nonlinear term  $\mathcal{N}(X^{(t)})$  can be neglected, being absorbed as a higher-order small quantity.

Neglecting the nonlinear term, the recursive relation for high-frequency energy simplifies to:

$$\|\mathcal{F}(X^{(t)})\|_{\Omega_H} \leq e^{-\gamma(\rho)\beta_0^2} \|\mathcal{F}(X^{(t-1)})\|_{\Omega_H} \quad (25)$$

Recursively, we obtain:

$$\|\mathcal{F}(X^{(t)})\|_{\Omega_H} \leq e^{-\gamma(\rho)\beta_0^2 t} \|\mathcal{F}(X^{(0)})\|_{\Omega_H} \quad (26)$$

Since  $\gamma(\rho) \geq \gamma_{\min} = \min_{\rho \in [0,1]} \gamma(\rho) > 0$ , the decay rate of high-frequency energy is bounded below by  $\gamma_{\min}\beta_0^2$ :

$$\|\mathcal{F}(X^{(t)})\|_{\Omega_H} \leq Ce^{-\gamma_{\min}\beta_0^2 t} \quad (27)$$

where  $C = \|\mathcal{F}(X^{(0)})\|_{\Omega_H}$  is a constant representing the initial high-frequency energy. Combining the upper bound of high-frequency energy and the lower bound of low-frequency energy, we have:

$$\frac{\|\mathcal{F}(X^{(t)})\|_{\Omega_H}}{\|\mathcal{F}(X^{(t)})\|_{\Omega_L}} \leq \frac{Ce^{-\gamma_{\min}\beta_0^2 t}}{c} \quad (28)$$

Since  $\gamma_{\min} > 0$  and  $\beta_0 > 0$ , the exponential term  $e^{-\gamma_{\min}\beta_0^2 t}$  approaches zero as  $t \rightarrow \infty$ . Therefore:

$$\lim_{t \rightarrow \infty} \frac{\|\mathcal{F}(X^{(t)})\|_{\Omega_H}}{\|\mathcal{F}(X^{(t)})\|_{\Omega_L}} = 0 \quad (29)$$



### CFG experiments on PiT

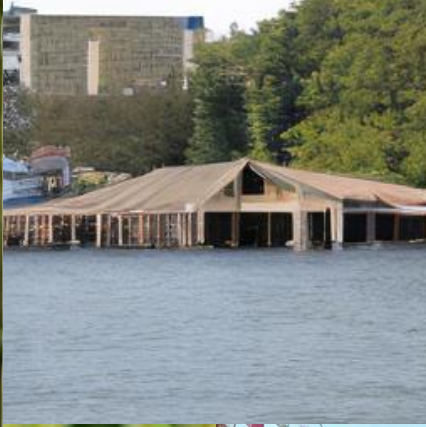
We conducted inference experiments with different Class-Free Guidance (CFG) under the same experimental settings, and the detailed results are shown in Table 1.

Model	FLOPs(G)	$FID_{CFG=1.0}$	$FID_{CFG=1.25}$	$FID_{CFG=1.5}$
DiT-XL/2*	114.46	19.86	7.64	5.28
PiT-B	<b>25.56</b>	<b>15.56</b>	<b>6.17</b>	<b>4.23</b>

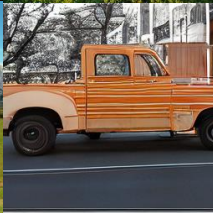
Table 9: Comparison of FID metrics between PiT-B and DiT-XL/2 under different CFG values.

### Supplementary of visualization

The following visualizations are the inference results of PiT-B after being trained for 400K steps at a 512x512 resolution. All images are from the ImageNet-1K dataset.



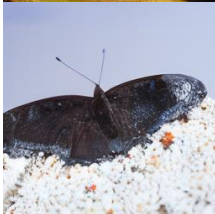
















## References

- Bao, F.; Nie, S.; Xue, K.; Li, C.; Pu, S.; Wang, Y.; Yue, G.; Cao, Y.; Su, H.; and Zhu, J. 2023. One transformer fits all distributions in multi-modal diffusion at scale. In *International Conference on Machine Learning*, 1692–1717. PMLR.
- Chen, C.-F. R.; Fan, Q.; and Panda, R. 2021. Crossvit: Cross-attention multi-scale vision transformer for image classification. In *Proceedings of the IEEE/CVF international conference on computer vision*, 357–366.
- Chen, H.; Wang, Y.; Guo, T.; Xu, C.; Deng, Y.; Liu, Z.; Ma, S.; Xu, C.; Xu, C.; and Gao, W. 2021. Pre-trained image processing transformer. In *Proceedings of the IEEE/CVF conference on computer vision and pattern recognition*, 12299–12310.
- Chen, J.; Yu, J.; Ge, C.; Yao, L.; Xie, E.; Wu, Y.; Wang, Z.; Kwok, J.; Luo, P.; Lu, H.; et al. 2023. Pixart-alpha: Fast training of diffusion transformer for photorealistic text-to-image synthesis. *arXiv preprint arXiv:2310.00426*.
- Chu, X.; Su, J.; Zhang, B.; and Shen, C. 2024. Visionllama: A unified llama interface for vision tasks. *arXiv e-prints*, arXiv–2403.
- Dai, Z.; Liu, H.; Le, Q. V.; and Tan, M. 2021. Coatnet: Marrying convolution and attention for all data sizes. *Advances in neural information processing systems*, 34: 3965–3977.
- Deng, J.; Dong, W.; Socher, R.; Li, L.-J.; Li, K.; and Fei-Fei, L. 2009. Imagenet: A large-scale hierarchical image database. In *2009 IEEE conference on computer vision and pattern recognition*, 248–255. Ieee.
- Dosovitskiy, A.; Beyer, L.; Kolesnikov, A.; Weissenborn, D.; Zhai, X.; Unterthiner, T.; Dehghani, M.; Minderer, M.; Heigold, G.; Gelly, S.; et al. 2020. An image is worth 16x16 words: Transformers for image recognition at scale. *arXiv preprint arXiv:2010.11929*.
- Esser, P.; Kulal, S.; Blattmann, A.; Entezari, R.; Müller, J.; Saini, H.; Levi, Y.; Lorenz, D.; Sauer, A.; Boesel, F.; et al. 2024. Scaling rectified flow transformers for high-resolution image synthesis. In *Forty-first international conference on machine learning*.
- Gao, S.; Zhou, P.; Cheng, M.-M.; and Yan, S. 2023a. Masked diffusion transformer is a strong image synthesizer. In *Proceedings of the IEEE/CVF international conference on computer vision*, 23164–23173.
- Gao, S.; Zhou, P.; Cheng, M.-M.; and Yan, S. 2023b. Mdtv2: Masked diffusion transformer is a strong image synthesizer. *arXiv preprint arXiv:2303.14389*.
- Hatamizadeh, A.; Song, J.; Liu, G.; Kautz, J.; and Vahdat, A. 2024. Diffit: Diffusion vision transformers for image generation. In *European Conference on Computer Vision*, 37–55. Springer.
- He, K.; Zhang, X.; Ren, S.; and Sun, J. 2016. Deep residual learning for image recognition. In *Proceedings of the IEEE conference on computer vision and pattern recognition*, 770–778.
- Ho, J.; Jain, A.; and Abbeel, P. 2020. Denoising diffusion probabilistic models. *Advances in neural information processing systems*, 33: 6840–6851.
- Liu, Z.; Guo, L.; Tang, Y.; Cai, J.; Ma, K.; Chen, X.; and Liu, J. 2025. VRoPE: Rotary Position Embedding for Video Large Language Models. *arXiv preprint arXiv:2502.11664*.
- Liu, Z.; Lin, Y.; Cao, Y.; Hu, H.; Wei, Y.; Zhang, Z.; Lin, S.; and Guo, B. 2021. Swin transformer: Hierarchical vision transformer using shifted windows. In *Proceedings of the IEEE/CVF international conference on computer vision*, 10012–10022.
- Lu, Z.; Wang, Z.; Huang, D.; Wu, C.; Liu, X.; Ouyang, W.; and Bai, L. 2024. Fit: Flexible vision transformer for diffusion model. *arXiv preprint arXiv:2402.12376*.
- Peebles, W.; and Xie, S. 2023. Scalable diffusion models with transformers. In *Proceedings of the IEEE/CVF international conference on computer vision*, 4195–4205.
- Rombach, R.; Blattmann, A.; Lorenz, D.; Esser, P.; and Ommer, B. 2022. High-resolution image synthesis with latent diffusion models. In *Proceedings of the IEEE/CVF conference on computer vision and pattern recognition*, 10684–10695.
- Ronneberger, O.; Fischer, P.; and Brox, T. 2015. U-net: Convolutional networks for biomedical image segmentation. In *Medical image computing and computer-assisted intervention—MICCAI 2015: 18th international conference, Munich, Germany, October 5-9, 2015, proceedings, part III* 18, 234–241. Springer.
- Shazeer, N. 2020. Glu variants improve transformer. *arXiv preprint arXiv:2002.05202*.
- Tian, Y.; Tu, Z.; Chen, H.; Hu, J.; Xu, C.; and Wang, Y. 2024. U-dits: Downsample tokens in u-shaped diffusion transformers. *arXiv preprint arXiv:2405.02730*.
- Touvron, H.; Cord, M.; Douze, M.; Massa, F.; Sablayrolles, A.; and Jégou, H. 2021. Training data-efficient image transformers & distillation through attention. In *International conference on machine learning*, 10347–10357. PMLR.
- Vaswani, A.; Shazeer, N.; Parmar, N.; Uszkoreit, J.; Jones, L.; Gomez, A. N.; Kaiser, Ł.; and Polosukhin, I. 2017. Attention is all you need. *Advances in neural information processing systems*, 30.
- Wang, W.; Xie, E.; Li, X.; Fan, D.-P.; Song, K.; Liang, D.; Lu, T.; Luo, P.; and Shao, L. 2021. Pyramid vision transformer: A versatile backbone for dense prediction without convolutions. In *Proceedings of the IEEE/CVF international conference on computer vision*, 568–578.
- Wu, H.; Xiao, B.; Codella, N.; Liu, M.; Dai, X.; Yuan, L.; and Zhang, L. 2021. Cvt: Introducing convolutions to vision transformers. In *Proceedings of the IEEE/CVF international conference on computer vision*, 22–31.
- Xu, Y.; Zhang, Q.; Zhang, J.; and Tao, D. 2021. Vitae: Vision transformer advanced by exploring intrinsic inductive bias. *Advances in neural information processing systems*, 34: 28522–28535.
- Yuan, L.; Chen, Y.; Wang, T.; Yu, W.; Shi, Y.; Jiang, Z.-H.; Tay, F. E.; Feng, J.; and Yan, S. 2021. Tokens-to-token vit: Training vision transformers from scratch on imagenet. In *Proceedings of the IEEE/CVF international conference on computer vision*, 558–567.

Zhang, J.; Hu, T.; He, H.; Xue, Z.; Wang, Y.; Wang, C.; Liu, Y.; Li, X.; and Tao, D. 2024. EMOv2: Pushing 5M Vision Model Frontier. *arXiv preprint arXiv:2412.06674*.

Zhang, J.; Li, X.; Li, J.; Liu, L.; Xue, Z.; Zhang, B.; Jiang, Z.; Huang, T.; Wang, Y.; and Wang, C. 2023. Rethinking mobile block for efficient attention-based models. In *2023 IEEE/CVF International Conference on Computer Vision (ICCV)*, 1389–1400. IEEE Computer Society.